11^{th} International Conference on Fracture Mechanics of Concrete and Concrete Structures
FraMCoS-11
J. M. Chandra Kishen, A. Ramaswamy, S. Ray and R. Vidyasagar (Eds)
https://doi.org/10.21012/FC11.092327

DISCRETE MODELING OF CONCRETE FAILURE AND SIZE-EFFECT

MADURA PATHIRAGE*, DANYANG TONG*, FLAVIEN THIERRY†, GIANLUCA CUSATIS*, DAVID GRÉGOIRE†, GILLES PIJAUDIER-CABOT†

*Northwestern University
Evanston, IL USA

†Universite de Pau et des Pays de l'Adour
Anglet, France

Key words: Lattice model, Fracture, Size-effect

Abstract. Size-effect defines the relation between the nominal strength at the onset of fracture and structural size. More generally, size-effect is interested in the variation of the mechanical response of geometrically similar structures. In order to simulate the size-effect, one needs to rely on numerical modeling to describe the formation, development and propagation of the fracture process zone. Although a number of models have been proposed over the years, a correct description of fracture and size-effect which accounts for boundary effects and varying structural geometry remains challenging. In this study, the Lattice Discrete Particle Model (LDPM) is used to investigate the effects of structural dimension and geometry on the nominal strength and fracturing process in concrete. LDPM simulates concrete at the aggregate level and has shown superior capabilities in simulating complex cracking mechanisms, thanks to the inherent discrete nature of the model. To provide a solid validation of LDPM, one of the most complete experimental data set available in the literature was considered and includes three-point bending tests on notched and unnotched beams. The model parameters were first calibrated on a single size notched beam under three-point bending and on the mechanical response under unconfined compression. LDPM was then used to perform blind predictions. The results show a very good agreement with the experimental data.

1 INTRODUCTION

Size-effect in quasi-brittle materials is a reduction in strength, observed when the structural size increases in geometrically similar structures. This phenomenon is well known for concrete (see for instance the work of [1–4]) and its importance was acknowledged in the civil engineering community, as it was for the first time incorporated in the most recent ACI standard in 2019 [5]. For concrete, simplified analytical formulations such as Bažant's size-effect law [6] only provide an approximate description of concrete scaling law. In order to account for the release of the stored energy in the fracture process zone (FPZ), and for the development and propagation of the fracture front for different specimen sizes and shapes, one must carry out accurate numerical simulations.

Several types of models have been proposed over the years to describe concrete fracture and size-effect. One can mention for instance the cohesive model [7], the crack-band model [8], non-local continuum damage models [9, 10], and discrete models [11]. In all the aforementioned formulations, two features are essential in capturing size-effect in strain softening materials such as concrete: (i) crack localization and (ii) existence of an internal characteristic

length related to the size of the heterogeneity. In continuum models, these two ingredients are phenomenologically defined through constitutive laws. In this respect, random lattice or particle models such as the ones described by [12] or [13] are considered superior. In this study, one of such models, namely the Lattice Discrete Particle Model (LDPM) [12, 14], which simulates concrete at the coarse aggregate level, is adopted.

In order to assess the capabilities of LDPM in simulating fracture and predicting size-effect, a comprehensive experimental data set on concrete fracturing [3] is considered. This data set is among one of the very few available in the literature that includes three-point bending tests on notched and unnotched beams and encompasses a large range of beam depths. This data set was previously used in several studies involving other numerical models. More specifically, an integral-type non-local model was used but was found ineffective in capturing correct size and geometry effects [3]. A lattice model [15] was able to simulate the data with a good accuracy. The model used in that study was bidimensional and, to the authors knowledge, there has been no attempt to extend the simulations to the 3D case.

More recently, a study proposed to simulate concrete fracturing using a local isotropic damage constitutive model of the Rankine type through the crack band model [16]. Although a good agreement with experimental data was found, this type of smeared crack model is limited in capturing complex cracking mechanisms and realistic crack tortuosity observed in concrete, which might have a non-negligible effect on energy dissipation during fracture. As a matter of fact, this effect is especially important in the case of unnotched beams where a large damage zone develops before collapsing into a single propagating crack that is ultimately tortuous.

Last but not least, a re-implementation of LDPM which includes stochasticity in material parameters was also used to simulate some of the data used in this paper [17] with a very good accuracy. It should be emphasized, however, that this study did not assess the capability of the model to predict size-effect.

In this work, the LDPM parameters were calibrated on a single beam configuration, leaving the remaining fracture test results for blind predictions, including splitting tests. It is our wish that this work would, to some extent, pave the way for more detailed and quantitative analyses of goodness of fits and prediction quality in future numerical studies within the concrete community, using the same set of experimental data and possibly other data. This would ultimately allow one to compare different model capabilities, develop the most effective models and abandon the less accurate ones.

The content of this paper has been presented in details in a recent paper [18]. The major results are summarized in the following.

2 LATTICE DISCRETE PARTICLE MODEL

This model, originally proposed by Cusatis and coworkers [12, 14], simulates the mechanical interactions among major material heterogeneities, i.e. coarse aggregates in concrete. Over the years, LDPM has been used to simulate quasi-brittle materials such as mortar [19, 20], fiber reinforced concrete and engineered cementitious composites [21–23], or cycling in concrete [24]. LDPM was also coupled to multi-physics models describing cement hydration from microscale simulations, heat transfer and mositure diffusion, alkali-silica reaction, creep, aging [25–28], or more recently self-healing in concrete [29].

2.1 Internal geometry

In order to generate the LDPM skeleton, spherical particles are placed in a volume of material from the largest to smallest size. This placement follows a prescribed particle size distribution that is based on the actual concrete mix design with the maximum and minimum aggregate sizes, d_a and d_0, respectively. Figure 1(a) shows an example of particle placement in a prismatic sample. In order to simulate the in-

teraction between particles, a lattice system is generated by means of a Delaunay tetrahedralization with the centers of particles. A dual tessallation is then performed which finally produces a system of polyhedral cells enclosing the spherical particles. Figure 1(b) shows an example of two adjacent polyhedral cells enclosing the spherical particles. The surface of each polyhedral cell is composed of triangular facets where failure can potentially occur. On each facet, stresses and strains are formulated in a vectorial form and related through constitutive equations. Figure 1(c) shows the three unit vectors defined at a generic facet colored in red, in the normal direction and in the two tangential directions. LDPM incorporates specific constitutive equations to describe tensile fracturing with strain softening, cohesive and frictional shearing, and compressive response with strain-hardening. Since this study focuses on concrete fracturing, the corresponding constitutive laws are recalled only.

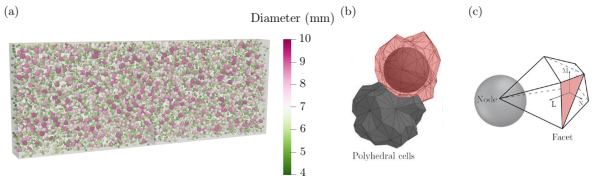

Figure 1: Fractured high strength concrete.

2.2 Elastic, tension, and tension-shear constitutive behaviors

If $\mathbf{x}_i$ and $\mathbf{x}_j$ denote the positions of nodes i and j, adjacent to the facet k, the facet strain vector is defined as:

$$\begin{aligned}\mathbf{e}_k &= [e_{N_k}\ e_{M_k}\ e_{L_k}]^t \\ &= \left[\frac{\mathbf{n}_k^t[\![\mathbf{u}_k]\!]}{l_k}\ \frac{\mathbf{m}_k^t[\![\mathbf{u}_k]\!]}{l_k}\ \frac{\mathbf{l}_k^t[\![\mathbf{u}_k]\!]}{l_k}\right]^t \end{aligned} \quad (1)$$

where e_{N_k} is the normal strain component, and e_{M_k} and e_{L_k} are the tangential strain components, $[\![\mathbf{u}_k]\!] = \mathbf{u}_j - \mathbf{u}_i$ is the displacement jump corresponding to facet k, $l_k = \|\mathbf{x}_j - \mathbf{x}_i\|$ is the distance between the two nodes, $\mathbf{n}_k = (\mathbf{x}_j - \mathbf{x}_i)/l_k$ and $\mathbf{m}_k$ and $\mathbf{l}_k$ are two unit vectors mutually orthogonal in the facet plane projected orthogonally to the line connecting the adjacent nodes.

The stress vector on facet k is defined as $\mathbf{t}_k = [t_{N_k}\ t_{M_k}\ t_{L_k}]^t$, where t_{N_k} is the normal component, and t_{M_k} and t_{L_k} are the shear components. For the sake of readability, the subscript k that designates the facet is further dropped. The elastic behavior is formulated through linear relations between the normal and shear stress vector components, and the corresponding strain vector components as follows:

$$t_N = E_N e_N\ ,\ t_M = E_T e_M\ ,\ t_L = E_T e_L \quad (2)$$

where $E_N = E_0$ and $E_T = \alpha_0 E_0$. $E_0 \approx E/(1-2\nu)$ and $\alpha_0 \approx (1-4\nu)/(1+\nu)$ are the effective normal modulus and the shear-normal coupling parameter, respectively. E is the macroscopic Young's modulus and ν is the macroscopic Poisson's ratio.

Because of the mesoscale nature of the model, concrete fracturing in mode I opening is always accompanied by shear at facets. This is a realistic feature since it is experimentally observed that most fracture paths are located at the interface between aggregates and cement paste. Therefore, the cohesive fracture behaviors in tension but also in tension-shear are important. This cohesive fracture occurs for $e_N > 0$. One can define an effective strain as $e = (e_N^2 + \alpha_0(e_M^2 + e_L^2))^{\frac{1}{2}}$, and an effective stress as $t = (t_N^2 + (t_M^2 + t_L^2)/\alpha_0)^{\frac{1}{2}}$ and write the relationship between stresses and strains through $t_N = te_N/e$, $t_M = \alpha_0 te_M/e$ and $t_L = \alpha_0 te_L/e$. The effective stress t is defined incrementally as $\dot{t} = E_N\dot{e}$ and its magnitude is limited by a strain-dependent boundary which is written as $0 \leqslant t \leqslant \sigma_{bt}(e, \omega_{sn})$ where

$$\begin{aligned}\sigma_{bt}(e,\omega_{sn}) &= \sigma_0(\omega_{sn}) \\ &\exp\left[-H_0(\omega_{sn})\frac{\langle e_{\max} - e_0(\omega_{sn})\rangle}{\sigma_0(\omega_{sn})}\right]. \end{aligned} \quad (3)$$

$\langle x\rangle = \max(x, 0)$, ω_{sn} is a variable defining the level of interaction between shear and normal loadings. It is defined as $\tan(\omega_{sn}) = (e_N)/(\sqrt{\alpha_0}e_T) = (t_N\sqrt{\alpha_0})/(t_T)$ where e_T is the total shear strain $e_T = (e_M^2 + e_L^2)^{\frac{1}{2}}$, and

t_T is the total shear stress $t_T = (t_M^2 + t_L^2)^{\frac{1}{2}}$. The maximum effective strain is time dependent and is defined as $e_{\max}(\tau) = (e_{N,\max}^2(\tau) + \alpha_0 e_{T,\max}^2(\tau))^{\frac{1}{2}}$ where $e_{N,\max}(\tau) = \max_{\tau'<\tau}[e_N(\tau')]$ and $e_{T,\max}(\tau) = \max_{\tau'<\tau}[e_T(\tau')]$. The strength limit of the effective stress that defines the transition between pure tension and pure shear is written as

$$\begin{aligned}\sigma_0(\omega_{sn}) &= \sigma_t \frac{-\sin(\omega_{sn})}{2\alpha_0 \cos^2(\omega_{sn})/r_{st}^2} \\ &+ \sigma_t \frac{(\sin^2(\omega_{sn}) + 4\alpha_0 \cos^2(\omega_{sn})/r_{st}^2)^{\frac{1}{2}}}{2\alpha_0 \cos^2(\omega_{sn})/r_{st}^2}\end{aligned} \quad (4)$$

where $r_{st} = \sigma_s/\sigma_t$ is the ratio of the shear strength to the tensile strength, σ_s is the shear strength and σ_t is the tensile strength. The post-peak softening modulus is controlled by the effective softening modulus in Eq. (3) $H_0(\omega_{sn}) = H_s/\alpha_0 + (H_t - H_s/\alpha_0)(2\omega_{sn}/\pi)^{n_t}$, in which $H_t = 2E_0/(l_t/l - 1)$, $H_s = r_s E_0$ and n_t is the softening exponent. Typically, the values of $n_t = 0.2$ and $r_s = 0$ are assumed and are fixed. l_t is the tensile characteristic length defined as $l_t = 2E_0 G_t/\sigma_t^2$ and G_t is the mesoscale fracture energy.

2.3 Static equilibrium equations and numerical implementation

The static linear and angular momentum equilibrium equations of each LDPM cell are written as follows:

$$\sum_{k\in\mathcal{F}_I} A_k^p \mathbf{t}_k = \mathbf{0}\ ,\ \sum_{k\in\mathcal{F}_I} A_k^p \mathbf{c}_k \times \mathbf{t}_k = \mathbf{0} \quad (5)$$

where $\mathcal{F}_I$ is the set containing all the facets of a generic polyhedral cell I, $A_k^p = A_k \mathbf{n}^t \mathbf{n}_k$ is the area of the projected facet k, $\mathbf{n}$ is the orientation of the tetrahedron edge associated to facet k and $\mathbf{n}_k$ is the unit vector orthogonal to facet k of area A_k [12]. $\mathbf{c}_k$ is the vector that represents the distance between the center of facet k and the center of the cell.

The model was implemented within a dynamic explicit scheme, with a central difference algorithm for time integration. Although the actual equations that are solved numerically are dynamic (see [12] for more details), loading rates were small enough to ensure the kinetic energy in the system would not exceed 5% of the internal energy throughout the analysis.

3 MODELING AND CALIBRATION

In the experimental work by [3], four sizes of geometrically similar prismatic specimens with four depths $D = 50$ mm, 100 mm, 200 mm, and 400 mm, span-to-depth ratio S/D of 2.5, and out-of-plane thickness of 50 mm were tested in three-point bending. Unnotched and notched samples with a notch length a and the notch-to-depth ratios $\alpha = a/D = 0.5, 0.2, 0$ were tested under CMOD control to obtain a stable post-peak response. In the case of unnotched beams, the extensometer was attached to the bottom surface of the beams, making sure that the major crack occured within the measurement zone of the extensometer. The data set also includes unconfined compression tests on cylindrical specimens and splitting tests. More details on the experimental program are given in Ref. [3].

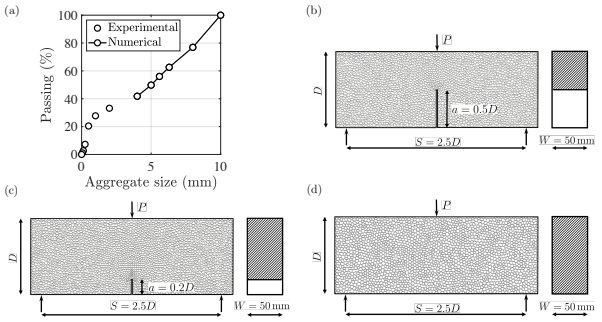

Figure 2: (a) Simulated particle size distribution, LDPM cells, geometries, and dimensions of the simulated beams with the notch-to-depth ratios of (b) 0.5, (c) 0.2, and (d) 0 viz. unotched beam.

The parameters required to construct the LDPM models were first identified based on the actual mix design used in the experiments. The particle size distribution was numerically reproduced following the procedure described in [28]

with a cut-off size $d_0 = 4$ mm and a maximum size $d_a = 10$ mm.

Figure 2(a) shows the experimental and numerical sieve curves. The remaining parameters were also chosen based on the mix design: cement content $c = 286$ kg m^{-3}, water-to-cement ratio $w/c = 0.626$, and density $\rho = 2121$ kg m^{-3}. Figure 2(b)-(d) show the simulated geometries and the resulting LDPM cells at the surface of the 3D samples.

3.1 Modeling and calibration process

The identification of the parameters in the constitutive laws describing elastic, tension, and tension-shear behaviors followed a two-step procedure. First, the normal modulus E_0 and α_0 related to the elastic behavior were calculated using the approximated formulas listed in Section 2.2, based on the mean values of the macroscopic elastic modulus and Poisson's ratio reported by [3]. The values of $E_0 = 57180$ MPa and $\alpha_0 = 0.25$ were obtained.

Next, the three parameters related to fracture and shear, i.e. the mesoscale tensile strength σ_t, the mesoscale fracture energy G_t, and the shear-to-tensile strength ratio r_{st} were identified simultaneously based on: (i) the compressive strength obtained from cylinders (diameter $D_c = 74$ mm and height $H_c = 142$ mm), and (ii) the load-CMOD curve corresponding to the medium size beam with the depth $D = 200$ mm and $\alpha = 0.2$. For the compression test, rigid plates were used on the top and bottom of the specimens. Friction between the plates and the sample was simulated through a simple Coulomb friction law with a friction coefficient $\mu = 0.13$. Concerning the bending test, the loads were applied directly on the surface nodes. Both compression and fracture tests were simulated under displacement control with a constant velocity of 1 mm s^{-1} to ensure quasi-static conditions. For each test, three simulations were performed with different spatial distributions of particles. The values of $\sigma_t = 2.9$ MPa, $G_t = 45.5$ N m^{-1}, and $r_{st} = 3.276$ were obtained after a simultaneous fit of the bending and compression tests.

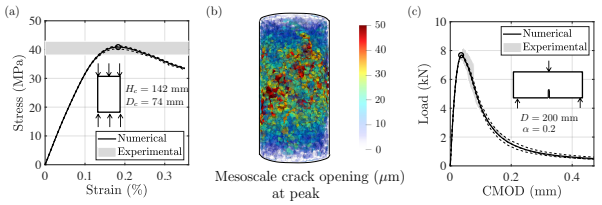

Figure 3: Calibration results: (a) stress-strain curve of the unconfined compression test; the empty circle designates the mean peak value, (b) failure mode at the peak load (c) load-CMOD curve of the three-point bending test on the notched beam with $D = 200$ mm and $\alpha = 0.2$.

Figure 3(a) shows the simulated stress-strain curve of the compression test together with the compressive strength obtained experimentally. The solid line is the mean curve of the three individual simulations. The gray area represents the experimental scatter where the upper and lower bounds of the envelope correspond to the maximum and minimum values of the strength, respectively. The mode of failure at peak is shown in Figure 3(b), characterized by a shear band. The LDPM facets are colored according to the value of the mesoscale crack opening defined as $w = (w_N^2 + w_M^2 + w_L^2)^{\frac{1}{2}}$ for $e_N > 0$ and $w = 0$ for $e_N < 0$, $w_i = l e_i^{ine}$ where $e_i^{ine} = e_i - t_i/E_i$ is the inelastic strain for $i = N, M, L$, and l is the edge length defined in Section 2.2. Figure 3(c) shows the experimental and numerical load-CMOD curves for the bending test.

The elastic behavior modeled by two parameters (E_0, α_0) and the mesoscale mixed mode fracture governed by three parameters (σ_t, G_t, r_{st}) have been now identified. Concrete failure is characterized by multiple mechanisms that are different and LDPM is able to simulate all these mechanisms. For each mechanism, there is a set of relevant model parameters (less than 4) which makes the total number of parameters to be 16. The remaining parameters that could not be fitted (because they correspond to failure mechanisms that are not relevant in the present experiments) were assumed based on the actual mix design and Section 5.3 by [14]: $\sigma_{c0} = 120$ MPa, $H_{c0}/E_0 = 0.4$, $k_{c0} = 2$, $k_{c1} = 1$, $k_{c2} = 5$, $\mu_0 = 0.2$, $\mu_\infty = 0$, $\sigma_{N0} = 600$ MPa, and $E_d/E_0 = 1$.

4 PREDICTIONS

LDPM was first validated on splitting tests for which peak loads for nine replicates are reported by [3]. For this purpose, three cylinders with the height $L_s = 215$ mm and the diameter $D_s = 113$ mm with different spatial distributions of particles were simulated. The load was applied directly on particles at the surface of the cylinder. In addition, the simulations were performed under displacement control with a constant loading rate of 1 mm s^{-1} to ensure quasi-static conditions.

Figure 4(a) shows the mean predicted nominal stress versus displacement curve represented by a solid line and the three individual simulations in dashed lines, along with the experimental scatter represented with a gray area.

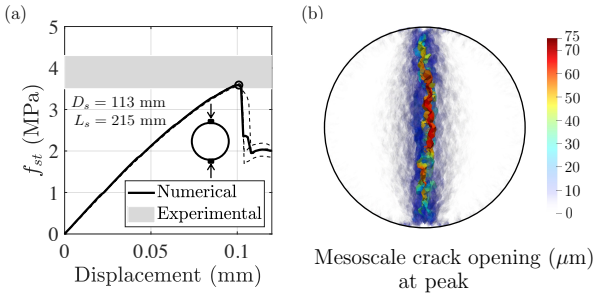

Figure 4: Prediction results: (a) nominal stress-displacement curve of the splitting test; the empty circle designates the mean peak value, and (b) failure mode at the peak load.

The nominal strength was computed using the formula $f_{st} = (2P_{st,u})/(\pi D_s L_s)$ where $P_{st,u}$ is the splitting peak force. One can observe that the numerical mean splitting tensile strength is within the scatter of the experiments. Figure 4(b) shows the mode of failure at the peak load. As expected, and in accordance with experimental observations, fracture initiates at the center where tensile stresses are the highest. The main crack is tortuous and has a slight eccentricity with respect to the vertical line passing through the center. This is due to the inherent ability of the mesoscale model to reproduce heterogeneity in the material.

The model was next used to predict the load-CMOD curves for all sizes and notch lengths. The simulations were performed under displacement control by applying loads at a constant loading rate of 1 mm s^{-1}.

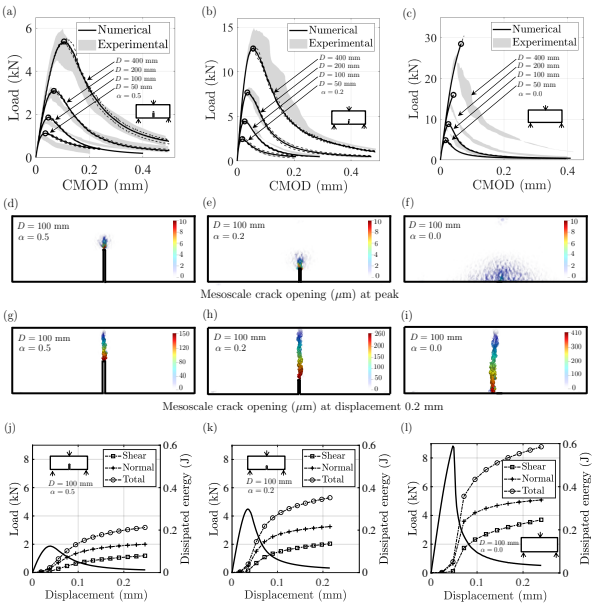

Figure 5: Prediction results: load-CMOD curves for (a) $\alpha = 0.5$, (b) $\alpha = 0.2$, (c) $\alpha = 0$, the empty circles designate mean peak values; failure modes at the peak load for the samples with the depth $D = 100$ mm for (d) $\alpha = 0.5$, (e) $\alpha = 0.2$, (f) $\alpha = 0$; failure modes at a displacement of 0.2 mm for the samples with the depth $D = 100$ mm for (g) $\alpha = 0.5$, (h) $\alpha = 0.2$, (i) $\alpha = 0$; dissipated energies for (j) $\alpha = 0.5$, (k) $\alpha = 0.2$, (l) $\alpha = 0$.

Figures 5(a)-(c) show the predicted curves for the notch-to-depth ratios of 0.5, 0.2, and 0, respectively. The solid line is the mean response of the three individual simulations in dashed lines. The experimental scatter is represented with a gray area. One can observe that the numerical simulations predict well the mechanical behavior in the elastic, near-peak and post-peak regimes for the different geometries and sizes. The prediction in the post-peak regime of the smallest size beam with a notch-to-depth ratio of 0.5 deviates from the experimental results. The reason might be that the number of aggregates in the ligament is not enough and makes the model too coarse. In addition, boundary effects play a significant role for such small specimens. In the case of the two unnotched beams with largest sizes, the response stops at the peak due to snapback, similarly to what was observed

in the experiments.

Figures 5(d)-(i) show the typical failure modes for the beams with the size $D = 100$ mm for two different displacement values. Two types of failure can be distinguished. (i) For the notched specimens, the FPZ is localized and emanates at the crack tip. It develops for the increasing load and finally reaches an ultimate size at the peak load (Figures 5(d) and (e)). The FPZ then propagates through the ligament (Figures 5(g) and (h)). (ii) For the unnotched specimens, the FPZ initiates at the bottom surface of the sample, where the stresses approach the material tensile strength, and is diffused on a zone much larger in size as compared to the notched-beam case. As the load increases up to the peak, the damaged zone becomes larger (Figure 5(f)). At the peak load a single crack propagates, whereas the surrounding material unloads. The final crack does not necessarily originate at mid-span. This phenomena shows the direct effect of material heterogeneity, realistically captured by the mesoscale model. Although not quantified here, the evolution of the FPZ is consistent with the one described in [30] based on Ripleys function analysis on the same experimental data.

As a matter of fact, the very nature of the model allows one to assess shear and tensile behaviors during fracture propagation. In general, the LDPM facets are subject to both tensile and shear strains even though the test configuration is designed for mode I opening. One can look at the evolution of the dissipated energy computed from the increment of the dissipated energy density $\dot{w}_d = 3(t_N \dot{e}_N^{ine} + t_M \dot{e}_M^{ine} + t_L \dot{e}_L^{ine})$ for $e_N > 0$ and the volume of the cell I containing the facet $V_I = (\sum_k A_k^p l_k)/3$. Summing over the entire volume of the sample, one can obtain the evolution in time (or displacement here) of the total dissipated energy W_d and dissociate the individual contributions of the normal component $W_{d,N}$ and the tangential components $W_{d,T}$. Figures 5(j)-(l) show the load-displacement curves for the beams with the size $D = 100$ mm for the three different notch lengths, together with the dissipated energies. As expected, the total energy dissipated at the end of the test/simulation is smaller for the larger notch length, i.e. for a smaller ligament length. This is consistent with the acoustic energy obtained from acoustic emission on the same type of experiments reported in the work of [31]. Moreover, one can observe a sharper increase in the dissipated energy as the notch length decreases, which is consistent with the increase in brittleness as α tends to zero. Up to the peak load, the energy dissipated in shear is negligible as compared to the one in tension, for all cases including the unnotched beam. However in the post-peak regime, the energy dissipated in shear becomes more than half of the energy dissipated in tension, which proves that the post-peak behavior involves both shear and tensile forces in the meso-structure.

5 UNIVERSAL SIZE-EFFECT LAW AND FRACTURE PARAMETERS

Macroscopic properties of concrete such as compressive or tensile strengths are usually determined in laboratory using standardized sample dimensions. On the other hand, size-effect tests applied in a certain range of sizes were shown to provide an accurate estimation of fracture properties [32]. This method is preferred to the work of fracture method that provides apparent fracture properties which are geometry and size dependent.

The size-effect method only requires the knowledge of peak loads and sample geometry. It appears therefore interesting to compare the fracture parameters obtained using experimental results as reported by [3] and parameters one could identify using the numerical predictions, keeping in mind that only one load-CMOD curve on a single size notched beam was sufficient for model calibration. In this study, the so-called Universal Size Effect Law (USEL) in its deterministic version [33] was considered. This fitting formula bridges Type I size-effect which occurs in structures that fail at crack initiation from a smooth surface and Type II size-effect occurring in notched structures. It also covers the two distinct asymptotic behav-

iors at large size in the typical double-logarithm nominal strength versus structural size representation: (i) $-1/2$ slope corresponding to linear elastic fracture mechanics for Type II size-effect and (ii) a straight horizontal line corresponding to the elastic limit for Type I size-effect. The formula is written as:

$$\sigma_{Nu} = \sqrt{\frac{EG_f}{g_0' c_f + g_0 D}} \left(1 - \frac{r c_f^2 g_0'' e^{-k\alpha^2}}{4(l_p + D)(g_0 D + g_0' c_f)}\right)^{1/r} \quad (6)$$

where $\sigma_{Nu} = (3P_u S)/(2WD^2)$ is the nominal strength corresponding to the peak load P_u, G_f is the fracture energy , and c_f is the effective length of the FPZ. $g_0 = g(\alpha_0)$ is the dimensionless energy release rate, and $g_0' = g'(\alpha_0)$ and $g_0'' = g''(\alpha_0)$ are its first and second derivatives, respectively, evaluated at the initial notch-to-depth ratios $\alpha_0 = 0.5, 0.2, 0$. Finally, r, k, and l_p are empirical constants.

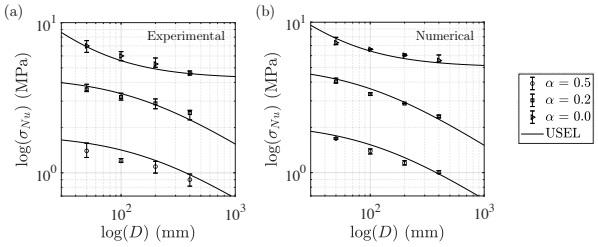

Figure 6: Fitting with the Universal Size Effect Law: nominal strength versus size for (a) experimental data and (b) simulation results.

Based on the expression of $g(\alpha)$ reported for example by [34] or [3], the following values were computed for the geometry studied in this paper: $g_0 = 2.96$, g_0' = 18.95, and g_0' = 153.88 for $\alpha = 0.5$, $g_0 = 0.57$, g_0' = 3.17, and g_0'' = 10.77 for $\alpha = 0.2$, and $g_0 = 0$, g_0' = 3.41, and g_0'' =-16.75 for $\alpha = 0$. By keeping the empirical constants $r = 0.11$, $k = 113$, and $l_p = 12.9$ identical to the ones reported in the work of [3], the model was fitted using the simulation data. The values of the fracture energy and effective length, $G_f = 39\,\mathrm{N\,m^{-1}}$ and $c_f = 16.8\,\mathrm{mm}$ were obtained. Figures 6(a)-(b) show the fitted model plotted together with the experimental and numerical data. These predicted fracture parameters are to be compared with the ones identified using the experimental results, i.e. $G_f = 42.6$ N m^{-1} and $c_f = 25.7$ mm [3]: both fracture energy and effective length can be qualitatively considered close enough with respect to the scatter of typical experiments on concrete. This result suggests that one could perform only one fracture test on a specific geometry in the laboratory, calibrate and use LDPM to simulate different sizes to identify the macroscale fracture energy and effective length of the FPZ through a size-effect law. In addition, the calibrated size-effect law could be used to obtain the nominal stresses of structures with various geometries.

6 CONCLUSIONS

In this study, a large set of experimental results on fracture and size-effect was simulated using the Lattice Discrete Particle Model (LDPM). The load-CMOD curve of a single size notched beam under three-point bending, and the compressive strength were used for model calibration. The remaining experimental results, namely one splitting test and eleven three-point bending tests of different beam sizes and notch lengths, were used for model validation without parameter adjustment.

The predictions on splitting tests and on the different beam geometries and sizes are overall in excellent agreement with the experimental data. The fracturing process is well captured by LDPM for both notched and unnotched beams. The dissipated energy in shear constitutes a large part of the total dissipated energy in the post-peak. Fracture parameters using the numerical results were identified through the Universal Size Effect Law (USEL) which can be predicted with a good accuracy.

7 ACKNOWLEDGMENTS

Partial financial support from the Investissement d'Avenir French program (ANR-16-IDEX-0002) under the framework of the E2S UPPA hub Newpores and from the Ezponda

project under the FEDER program is gratefully acknowledged. This research was also performed with the help from the computational resources provided for the Quest high performance computing facility at Northwestern University, which is jointly supported by the Office of the Provost, the Office for Research, and Northwestern University Information Technology.

REFERENCES

[1] Z.P. Bažant and P.A. Pfeiffer. Determination of fracture energy from size effect and brittleness number. *ACI Materials Journal*, 84(6):463–480, 1987.

[2] C.G. Hoover, Z.P. Bažant, J. Vorel, R. Wendner, and M.H. Hubler. Comprehensive concrete fracture tests: description and results. *Engineering Fracture Mechanics*, 114:92–103, 2013.

[3] D. Grégoire, L.B. Rojas-Solano, and G. Pijaudier-Cabot. Failure and size effect for notched and unnotched concrete beams. *International Journal for Numerical and Analytical Methods in Geomechanics*, 37(10):1434–1452, 2013.

[4] Y. Çağlar and S. Şener. Size effect tests of different notch depth specimens with support rotation measurements. *Engineering Fracture Mechanics*, 157:43–55, 2016.

[5] ACI-Committee. Building code requirements for structural concrete (aci 318-19) and commentary. American Concrete Institute, 2019.

[6] Z.P. Bažant. *Scaling of Structural Strength*. CRC Press, 2002.

[7] M. Elices, G.V. Guinea, J. Gomez, and J. Planas. The cohesive zone model: advantages, limitations and challenges. *Engineering Fracture Mechanics*, 69(2):137–163, 2002.

[8] Z.P. Bažant and B.H. Oh. Crack band theory for fracture of concrete. *Materials and Structures*, 16(3):155–177, 1983.

[9] G. Pijaudier-Cabot and Z.P. Bažant. Nonlocal damage theory. *Journal of engineering mechanics*, 113(10):1512–1533, 1987.

[10] Z.P. Bažant and M. Jirásek. Nonlocal integral formulations of plasticity and damage: survey of progress. *Journal of Engineering Mechanics*, 128(11):1119–1149, 2002.

[11] J.E. Bolander, J. Eliáš, G. Cusatis, and K. Nagai. Discrete mechanical models of concrete fracture. *Engineering Fracture Mechanics*, 257:108030, 2021.

[12] G. Cusatis, D. Pelessone, and A. Mencarelli. Lattice discrete particle model (ldpm) for failure behavior of concrete. i: Theory. *Cement and Concrete Composites*, 33(9):881–890, 2011.

[13] J. Eliáš, M. Vořechovskỳ, J. Skoček, and Z.P. Bažant. Stochastic discrete meso-scale simulations of concrete fracture: Comparison to experimental data. *Engineering Fracture Mechanics*, 135:1–16, 2015.

[14] G. Cusatis, A. Mencarelli, D. Pelessone, and J. Baylot. Lattice discrete particle model (ldpm) for failure behavior of concrete. ii: Calibration and validation. *Cement and Concrete Composites*, 33(9):891–905, 2011.

[15] P. Grassl, D. Grégoire, L. Rojas-Solano, and G. Pijaudier-Cabot. Meso-scale modelling of the size effect on the fracture process zone of concrete. *International Journal of Solids and Structures*, 49(13):1818–1827, 2012.

[16] G.B. Barbat, M. Cervera, M. Chiumenti, and E. Espinoza. Structural size effect: Experimental, theoretical and accu-

rate computational assessment. *Engineering Structures*, 213:110555, 2020.

[17] J. Eliáš and M. Vořechovskỳ. Fracture in random quasibrittle media: I. discrete mesoscale simulations of load capacity and fracture process zone. *Engineering Fracture Mechanics*, 235:107160, 2020.

[18] M. Pathirage, D. Tong, F. Thierry, G. Cusatis, D. Grégoire, and G. Pijaudier-Cabot. Discrete modelling of failure and size effect. *Theoretical and Applied Fracture Mechanics*, 124(103738), 2023.

[19] M. Pathirage, F. Bousikhane, M. D'Ambrosia, M. Alnaggar, and G. Cusatis. Effect of alkali silica reaction on the mechanical properties of aging mortar bars: Experiments and numerical modeling. *International Journal of Damage Mechanics*, 28(2):291–322, 2019.

[20] L. Han, M. Pathirage, A.T. Akono, and G. Cusatis. Lattice discrete particle modeling of size effect in slab scratch tests. *Journal of Applied Mechanics*, 88(2), 11 2020. 021009.

[21] E.A. Schauffert and G. Cusatis. Lattice discrete particle model for fiber-reinforced concrete. i: Theory. *Journal of Engineering Mechanics*, 138(7):826–833, 2011.

[22] Roozbeh Rezakhani, Dylan A Scott, Faysal Bousikhane, Madura Pathirage, Robert D Moser, Brian H Green, and Gianluca Cusatis. Influence of steel fiber size, shape, and strength on the quasi-static properties of ultra-high performance concrete: Experimental investigation and numerical modeling. *Construction and Building Materials*, 296:123532, 2021.

[23] J. Feng, W. Sun, L. Chen, B. Chen, E. Arkin, L. Du, and M. Pathirage. Engineered cementitious composites using chinese local ingredients: Material preparation and numerical investigation. *Case Studies in Construction Materials*, 16:e00852, 2022.

[24] Z. Zhu, M. Pathirage, W. Wang, M. Troemner, and G. Cusatis. Lattice discrete particle modeling of concrete under cyclic tension–compression with multi-axial confinement. *Construction and Building Materials*, 352:128985, 2022.

[25] M. Alnaggar, G. Cusatis, and G. Di Luzio. Lattice discrete particle modeling (ldpm) of alkali silica reaction (asr) deterioration of concrete structures. *Cement and Concrete Composites*, 41:45–59, 2013.

[26] M. Pathirage, D.P. Bentz, G. Di Luzio, E. Masoero, and G. Cusatis. The onix model: a parameter-free multiscale framework for the prediction of self-desiccation in concrete. *Cement and Concrete Composites*, 103:36–48, 2019.

[27] L. Yang, M. Pathirage, H. Su, M. Alnaggar, G. Di Luzio, and G. Cusatis. Computational modeling of temperature and relative humidity effects on concrete expansion due to alkali–silica reaction. *Cement and Concrete Composites*, 124:104237, 2021.

[28] L. Yang, M. Pathirage, H. Su, M. Alnaggar, G. Di Luzio, and G. Cusatis. Computational modeling of expansion and deterioration due to alkali–silica reaction: Effects of size range, size distribution, and content of reactive aggregate. *International Journal of Solids and Structures*, 234-235:111220, 2022.

[29] A. Cibelli, M. Pathirage, G. Cusatis, L. Ferrara, and G. Di Luzio. A discrete numerical model for the effects of crack healing on the behaviour of ordinary plain concrete: Implementation, calibration, and validation. *Engineering Fracture Mechanics*, 263:108266, 2022.

[30] V. Lefort, G. Pijaudier-Cabot, and D. Grégoire. Analysis by ripley's function of the correlations involved during failure in quasi-brittle materials: Experimental and numerical investigations at the mesoscale. *Engineering Fracture Mechanics*, 147:449–467, 2015.

[31] D. Grégoire, L. Verdon, V. Lefort, P. Grassl, J. Saliba, J.P. Regoin, A. Loukili, and G. Pijaudier-Cabot. Mesoscale analysis of failure in quasi-brittle materials: comparison between lattice model and acoustic emission data. *International Journal for Numerical and Analytical Methods in Geomechanics*, 39(15):1639–1664, 2015.

[32] Draft Recommendation RILEM. Size-effect method for determining fracture energy and process zone size of concrete. *Materials and Structures*, 23:461–465, 1990.

[33] Z.P. Bažant and Q. Yu. Universal size effect law and effect of crack depth on quasi-brittle structure strength. *Journal of Engineering Mechanics*, 135(2):78–84, 2009.

[34] Z.P. Bažant and J. Planas. *Fracture and Size Effect in Concrete and Other Quasibrittle Materials*. CRC press, 1997.